

Configuration jumps of rotor in a nanomotor from carbon nanostructures



Kun Cai ^{a,b,**}, Jingzhou Yu ^a, Jing Wan ^a, Hang Yin ^a, Jiao Shi ^a, Qing H. Qin ^{b,*}

^a College of Water Resources and Architectural Engineering, Northwest A&F University, Yangling 712100, China

^b Research School of Engineering, The Australian National University, Canberra, ACT 2601, Australia

ARTICLE INFO

Article history:

Received 1 December 2015

Received in revised form

20 January 2016

Accepted 26 January 2016

Available online 29 January 2016

ABSTRACT

Measuring the rotation of a rotor in a thermally driven motor made from double-wall carbon nanotubes (DWCNTs) involves challenges based in the small size of the nanotube (radius usually being less than or equal to 5 nm) and the high frequency of rotation (over 100 GHz). These features motivated us to study a rotor with variable configurations, in which the rotor is fabricated initially by bonding a graphene (GN) nanoribbon on a carbon nanotube (CNT). The width of the GN nanoribbon is far greater than the radius of the CNT. Using molecular dynamics simulation, we find that the "CNT + GN" rotor generally experiences three representative stages. In the first stage, the GN nanoribbon winds onto the CNT and the rotor becomes a carbon nanoscroll (CNS) within 100 ps (picoseconds). The second stage is acceleration of the rotor's rotation. The duration of that stage is controlled by the number of inward radial deviation (IRD) carbon atoms on the stator and the inertial moment of the rotor. When the rotational speed of the CNT reaches a critical value, the CNS unwinds within 80 ps into a nanoribbon, which can be considered as the third stage. When hydrogen atoms are initially added to the GN, more configuration variations of the rotor can be identified. The rotation of the "CNT + GN" rotor can be feasibly measured by observing the configuration variations of the rotor.

© 2016 Elsevier Ltd. All rights reserved.

1. Introduction

Carbon nanostructures are commonly formed with sp^2 and/or sp^3 carbon atoms. According to their dimensions, nanostructures are classified as zero-dimensional, e.g., buckyball ([1]); one-dimensional, e.g., CNT ([2]), CNS ([3,4]); two-dimensional, e.g., graphene ([5,6]), or graphite ([7]); and naturally three-dimensional structures, e.g., diamond, and complex three-dimensional structures made from lower dimensional nanostructures ([8]). These nanostructures have attracted much attention in the last two decades due to the unique mechanical properties ([6,9]) within each individual nanostructure and the ultra-weak interaction between adjacent tubes and/or graphene (GN) nanoribbons ([10,11]). Consequently, carbon nanostructures have been considered important candidate components in next-

generation nano/micro-electromechanical systems (NEMS/MEMS) ([12,13]) and nano devices, such as nanomotors ([14–16]), nano bearings ([17]), sensors ([18,19]) and so on.

Among nano devices, CNT-based nanomotors have attracted much attention in recent years. For example, Barreiro, Rurali et al. [14] confirmed the rotary and translational motions along the tube axis between the tubes in a multi-wall carbon nanotube (MWCNT) by experimentation. They demonstrated that the motion was actuated by the interaction among atoms on the tubes with a thermal gradient. More evidence can also be found in the work of [15] and of [16]. These experiments displayed the same 2 characteristics. First, the motions were of low velocity. Secondly, the size of the nano device was around a few hundred nanometers (nm). Even now, it is still difficult experimentally to investigate ([20]) the dynamic behaviors, namely rotation and oscillation, of a high-frequency (over 1 GHz) rotary nanomotor not more than 20 nm in size. To prove the theoretical investigation of small motors with over 1 GHz rotational frequency, molecular dynamics (MD) simulation seems to be the most favored method. Using simulation, many schemes, such as electric field ([21–23]), gas or liquid flow ([24,25]), and thermal vibration or light absorption, have been

* Corresponding author.

** Corresponding author. Research School of Engineering, The Australian National University, Canberra, ACT 2601, Australia.

E-mail addresses: kuncai99@163.com (K. Cai), qinghua.qin@anu.edu.au (Q.H. Qin).

proposed to drive the rotation of a nanotube in a MWCNT-based bearing.

In particular, thermal vibration of atoms in MWCNTs with fixed outer shells can also result in the rotation of free inner shells. The first result was mentioned briefly in the work of ([26]), who investigated the large amplitude axial oscillation of the inner tube in a DWCNT at a finite environmental temperature. In 2014 ([27]), we gave a definite answer as to the existence of a rotary CNT-based nanomotor in a NVT ensemble with a constant temperature (rather than a varying temperature or a temperature with a gradient along the tube axis).

The finding of a uniform temperature driven CNT-based nanomotor inspired measurement of the rotational speed of the rotor for two major reasons. The first is that the rotational speed of the rotor is too high, that is, generally greater than 100 GHz. Common video devices cannot capture the real motion of such a rotor. The other reason is that the rotor has a very small radius, making it difficult to capture variations of its configuration. To overcome these difficulties, the radial size of the rotor needs to be enlarged, for example, by bonding a piece of GN nanoribbon on the inner tube. In that model, the nanomotor has a “CNT + GN” rotor. However, if the configuration of the “CNT + GN” rotor remains unchanged, it is still difficult to measure the rotor's rotational speed. Fortunately, GN bonded with an inner tube (CNT) has a variable configuration due to van der Waals interaction. Moreover, the GN nanoribbon wound on the CNT can also be unwound from the CNT when the rotational speed is sufficiently high ([28]). If the change in the configuration can be observed, the rotation of the rotor can also be found. In the present study, we use a MD simulation approach to verify the feasibility of measuring the rotation of the rotor in a DWCNT-based motor.

2. Models and methods

In the thermal motor model shown in Fig. 1, the inner tube ((9, 9) CNT) will be driven to rotate if the configuration of the stators ((14, 14) CNT) is not symmetric axially, where the outer tubes are fixed as stators. To express the non-symmetry of a stator, we measure the IRD value of an end atom on the stator and label it “ Δr ”. Concretely, the atom has “ Δr ” of displacement along the dash line (See the four enlarged sub-figures below in Fig. 1 labeled with 1, 2, 3 and 4) from

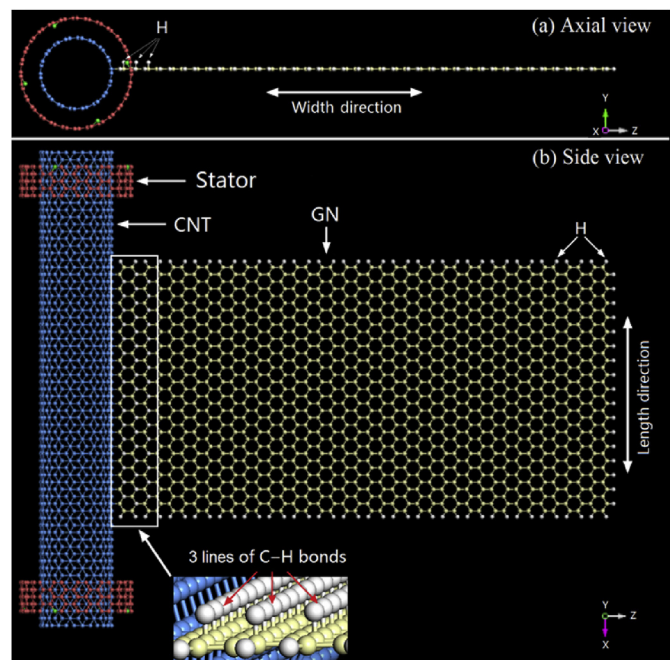


Fig. 2. Initial model of thermal motor with the CNT + GN rotor. (a) Axial view; (b) Side view. The tubes in the thermal motor are the same as those in Fig. 1 and a GN (light yellow atoms) $8.4 \text{ nm} \times 4.2 \text{ nm}$ is symmetrically bonded on the inner tube (blue atoms/CNT). Each carbon atom on the three free sides of the GN is bonded with a hydrogen (white) atom. Near the contact side between the CNT and GN along the axial/x-direction, on the GN, q lines (parallel axis of inner tube) of carbon atoms are hydrogenated, so in the present model, $q = 3$. (A colour version of this figure can be viewed online.)

its initial position on the ideal circle. In the present study, we set $\Delta r = 0.4l_{c-c}$ for all simulations, where $l_{c-c} = 0.142 \text{ nm}$, i.e., the bond length between two carbon atoms on the GN. If all the atoms on the stators have no IRD, the axial view of a stator is an ideal circle. Mathematically, the distance between the IRD atom and its neighbor carbon atom is $1 + \alpha^2$ times of l_{c-c} , where α is the ratio of Δr over l_{c-c} . When $\alpha = 0.4$, the bond length is 1.077 times of l_{c-c} . Suggestion is that α is less than 0.7.

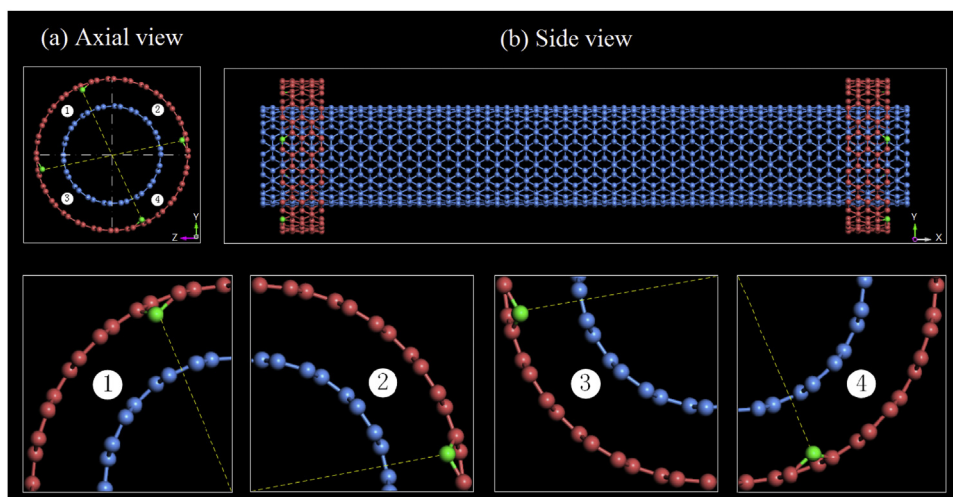


Fig. 1. A thermal nanomotor is made from a (9, 9)/(14, 14) DWCNT in which the inner tube (CNT rotor) is free and the two stators are fixed in simulation. The axial distance between two stators is 6.642 nm. The initial axial distance between the outer ends of the stator and the CNT rotor is 0.246 nm. (a) Axial view of motor. On each outer end of the stator are 4 atoms with IRD. Briefly, this stator is called a “4-IRD-atom” stator. (b) Side view of the motor. Below are four sub-figures for showing the IRD atoms clearly. (A colour version of this figure can be viewed online.)

Based on the motor model shown in Fig. 1, a complicated motor model is presented in Fig. 2. In the model, the rotor consists of the original (9, 9) CNT bonded with a piece of GN nanoribbon. The other three boundaries of the GN nanoribbon is passivated with hydrogen (H) atoms, i.e., each boundary carbon atom on GN is bonded with a H-atom. Nearby the connecting boundary, the internal carbon atoms on GN may be bonded with hydrogen atoms so as to curve the ribbon at initial stage.

The detailed parameters of the two models are found in Table 1.

LAMMPS ([29,30]) software is adopted in the present study for the following simulations. The AIREBO potential proposed by Stuart et al. ([31]), is chosen to describe the interaction among atoms in the carbon-hydrogen (C–H) system. It is popular in MD simulations for C–H system ([8,32–34]).

In the present simulations, the three items of AIREBO potential, e.g., REBO, Lennard-Jones (L-J) and torsion, are chosen with the cut-off of L-J potential being 1.02 nm. The initial model shown in Figs. 1 and 2 are reshaped by energy minimization, in which the steepest descending (SD) algorithm is used. After energy minimization, the two stators are fixed and the rotor is at canonical NVT ensemble with T = 300 K. The time step is 0.001 ps for the update of positions and velocity of atoms. Simulation steps are not less than 3 million.

3. Results and discussion

3.1. Thermally driven motor made from CNTs

Fig. 3 shows the rotational frequency of an inner tube excited by interaction between tubes of an NVT ensemble with T = 300 K. During simulation, all atoms on the stators are fixed. Due to thermal vibration of the atoms at the end of the inner tube (CNT rotor), the interaction between the inner tube and the atoms with IRD on the stator can drive the inner tube to rotate along the axis ([27]). Especially, the end carbon atoms have higher potential than the internal atoms ([37]). If no end atom on the stators has IRD, the inner tube is not excited to rotate (0 atom/black line in Fig. 3). If 2 atoms on each stator have IRD (orange line), the inner tube is driven to rotate quickly. After 1000 ps, the rotational frequency of the inner tube reaches ~170 GHz, and the rotational speed increases further after 2500 ps. If there are 4 atoms with IRD on each outer tube (blue line), the rotational frequency exceeds 200 GHz after 500 ps and approaches ~895 GHz at 1233 ps. But suddenly, the rotational speed drops to a few GHz at 1254 ps and varies near zero on time average ([38]). It is known that the radius of the inner tube increases with an increase of rotational speed due to the centrifugal effect ([39]). The inner tube seeks to be bonded with a stator through the carbon atoms on its ends and the IRD atoms on the stator.

From the results shown in Fig. 3, we believe that the rotational speed of the inner tube can be specified by changing such factors as the values of Δr or the number of end atoms with IRD on the stators. More atoms with IRD on a stator result in higher acceleration of the rotor.

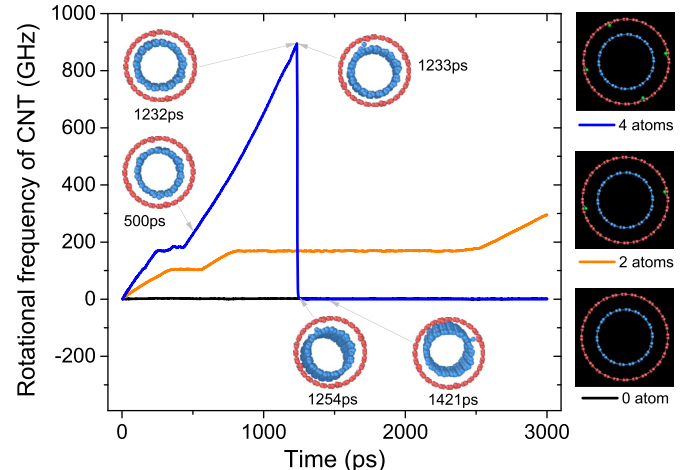


Fig. 3. Histories of (anti-clockwise) rotational frequency of the inner tube (CNT) in starters with different IRD schemes. (a) Black line/0 atom: outer tubes are ideal tubes; (b) Orange line/2 atoms: 2-IRD-atom stator; (c) Blue line/4 atoms: 4-IRD atom stator. 5 snapshots are inserted. The environmental temperature is 300 K. (A colour version of this figure can be viewed online.)

During rotating, the rotor also oscillates along x-axis ([27]). But the amplitude of oscillation is less than 0.246 nm. The reason is that the tube ends has higher potential barrier ([37]).

3.2. Thermally driven motor with CNT+GN rotor

In Fig. 4, the width of the GN is 14.8 nm. In the first ~80 ps, the difference between the rotational speeds of the CNT and GN is obvious. During that period, the rotational speed is no higher than 25 GHz, and the GN winds around the CNT step by step (see Fig. 4(a)).

In Fig. 4(b), it is evident from the configurations of the rotor at 79 and 531 ps that the GN/CNS attaches on the CNT stably. When the rotational speed of the CNT reaches ~90 GHz at 997 ps, near the contact side of the GN, the distance between the CNT and GN increases suddenly. This jump indicates that the interaction between the CNT and GN is reduced. Although the CNS/GN remains enclosed at this moment, the stability of the rotor's configuration disappears because the configuration changes quickly in the next few ps. For example, at 1002 ps, the axial free side of the GN is distant from CNT. At 1014 ps, the GN expands further and changes almost to its original shape. From 997 to 1014 ps, the rotational speeds of both CNT and GN jump to a very low value. In particular, the mean of rotation speed over the time interval [1020, 1050] ps is almost zero. Subsequently, the GN nanoribbon becomes more flattened and the rotor rotates along the axis like a second hand. The rotational speed does not exceed 20 GHz before 3000 ps. Hence, we conclude that the rotor's rotation can be most easily measured in the present conditions, i.e., when the radial size of the rotor is large and the

Table 1

Geometric parameters of the thermal motor systems involved in the present study (length unit: nm).

Name	Rotor	Stator	GN nanoribbon					
Length (x)	8.1164	0.4919	4.2	4.2	4.2	4.2	4.2	4.2
Diameter/width (z)	1.2204	1.8984	14.8	14.8	8.4	5.8	5.4	4.5
Number of atoms	1206C**	140C	2450C +157H +Extra	2450C +157H +Extra	1400C +97H +Extra	980C +73H +Extra	910C +69H +Extra	770C +61H +Extra

**: "C" represents carbon atoms; "H" represents hydrogen atoms; "Extra" hydrogen atoms are bonded with internal carbon atoms on GN, for different lines of C–H bonds, the numbers of H-atoms are different, e.g., 0(0 line), 33(2 lines), 49(3 lines), 82(5 lines) and 165 (10 lines).

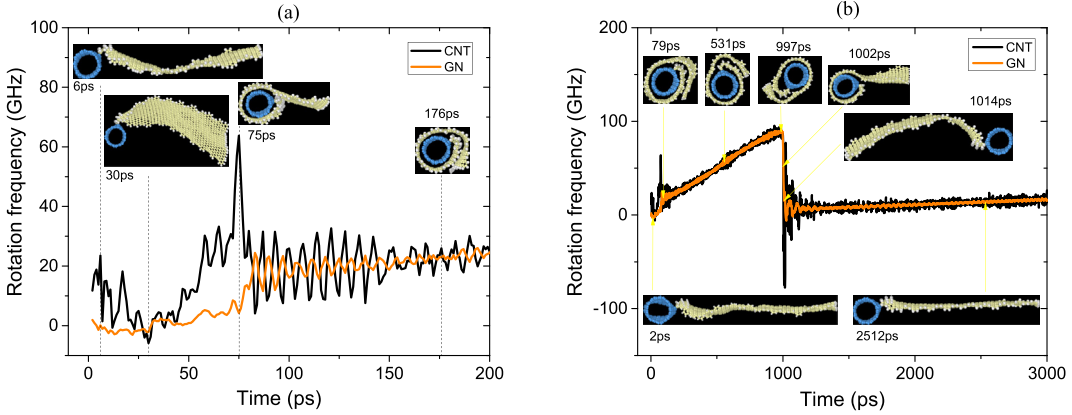


Fig. 4. Histories of rotational frequency of CNT and GN/CNS in the model shown in Fig. 2 at 300 K. (a) During [0, 200] ps with 4 snapshots at 6, 30, 75, and 176 ps (Movie M1); (b) During [0, 3000] ps with 7 snapshots at 2, 79, 531, 997, 1002, 1014, and 2512 ps (Movie M2). The angular velocity of the GN is counted by the time-averaged angular velocities of atoms in the GN with respect to its center of mass along the x-direction. (A colour version of this figure can be viewed online.)

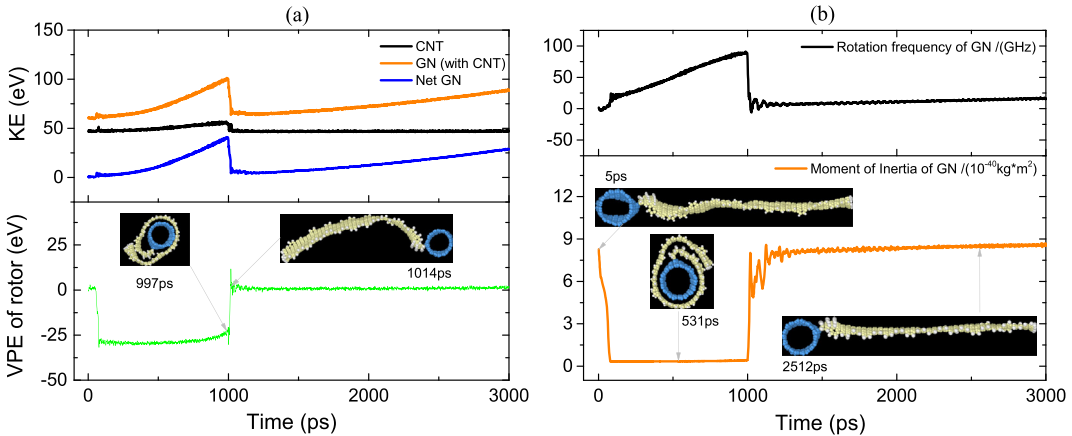


Fig. 5. Histories of energy and moment of inertia. (a) Kinetic energy (KE), including CNT (black line: KE of the inner tube/CNT), GN (orange line: total KE of GN), Net GN (blue line: subtract the thermal vibration KE from the total KE of GN), and (green line) variation of potential energy (VPE) of rotor with reference value of -21,230.8 eV. The difference between the GN and Net GN curves indicates that temperature is well controlled. (b) Moment of inertia of GN with respect to axis of CNT. (A colour version of this figure can be viewed online.)

rotational speed is low.

From the KE curves shown in Fig. 5(a), we find that the KE of both the CNT and the GN exhibits a jump near 1000 ps. Soon afterwards, both KEs increase, the KE of the GN increasing more quickly than that of the CNT due to their identical rotational speed (ω) but different moments of inertia (I_z) (and $KE = 0.5I_z\omega^2$). In fact, there is a small jump during [0, 79] ps. That jump is not shown clearly in Fig. 5(a) because of the low rotational speeds of the CNT and GN. From the VPE history, two jumps can be identified, a jump down during [0, 79] ps and a jump up during [997, 1014] ps. The first jump of potential energy is caused by the winding of the GN from nanoribbon to scroll, causing the surface energy of the rotor to reduce. The second jump is caused by the unwinding of the GN from scroll to nanoribbon.

From Fig. 5(b), we can also find a trap in the moment of inertia of the GN during simulation. But the mechanism of this trap is different from that shown in the lower layer of Fig. 5(a). As we know, $I_z = \sum_{i=1}^N m_i r_i^2$, where m_i is the mass of the i -th atom and r_i is the distance between the atom and the axis of the CNT, N is the total number of atoms in the GN. The jump down of I_z during [0, 79] ps is the result of the winding of GN from nanoribbon to scroll, leading to the decrease of r_i . In contrast, the jump up of I_z during [997, 1014] ps is the result of the unwinding of GN from CNS to nanoribbon.

During the period, the distance between the atoms in the GN and the axis of the CNT increases. The value of I_z also increases after 1200 ps, because the radial tension within the GN plane increases with the increase in rotational speed of the CNT.

Two questions may arise.

One question is: Why the “CNT + GN” rotor is in a stable rotating state while the CNT rotor fails (in Fig. 3)?

From the results listed in Figs. 3 and 4, one can find that the rotor made of CNT + GN rotates far slower than that made just a CNT. For example, the rotational frequency of the “CNT + GN” rotor is lower than 100 GHz, while the rotor which fails after 1232 ps (blue line in Fig. 3) rotates at ~895 GHz. Hence, the end carbon atoms on the CNT rotor have large outward radial deviation at such high rotational frequency. Both centrifugal force and thermal vibration increases failure of rotation due to new C–C bond formed between the rotor and stator. It is also known that the centrifugal force is proportional to the radius, but proportional to the square of rotational frequency. That is the reason why the CNT rotor is unstable while the “CNT + GN” rotor is stable experiencing a longer period. It is predictable that the “CNT + GN” rotor may also fail to rotate if its rotational speed is too high, e.g., >500 GHz which needs over 100 ns of acceleration (Fig. 4(b)).

The other question is: Why can't the GN wind into a CNS again

after the second jump (after 1020 ps)?

To answer this question, we investigate the status of the GN in the initial stage, i.e., [0, 30] ps and after the second jump. In the initial stage, the GN has a small negative rotational speed, caused by the curling of GN near the C–H bond lines. During that period, adjustment of the angle between the C–H and the GN plane leads to a decrease in the potential energy of the system. Simultaneously, the CNT has a very low positive speed, which has the advantage of decreasing the distance between the middle part of the GN and the CNT to form a CNS on the CNT. Hence, within 100 ps, the GN is changed to a CNS. In the stage after 1000 ps, the rotational speed of the CNT jumps down to a few GHz and the averaged rotational speed of the GN is also very low. But the outer part of the GN still rotates at a high positive speed, and its rotational direction is opposite to that of the curling direction of GN from nanoribbon to CNS. Meanwhile, Fig. 6 illustrates that the tension between the CNT (black ball) and the GN (blue balls) depends strongly on both the distance between the CNT axis (point "z") and the atoms in GN and the rotational speed of the GN (ω). As the tension within the GN is high enough to prevent curling of the GN due to the C–H bond, the GN has no opportunity to wind into a CNS on the CNT again.

3.3. Effects of C–H scheme on configuration of rotor jumps

In the previous simulation, $q = 3$, i.e., there are three lines of carbon atoms in the GN near the contact side, and they are bonded by hydrogen atoms. It is known that the C–H bonds on the GN will reshape the nanoribbon ([7,8,34–36,40]). The above simulation also supports this conclusion. If we change the value of q , what will happen to the configuration of the CNT + GN rotor? To demonstrate the effect of q , we set q to be 0, 2, 3, 5, and 10, successively. " $q = 0$ " implies that no hydrogen atom is bonded with internal carbon atoms in GN. " $q = 2$ " means that only two adjacent lines of carbon atoms in the GN are bonded with hydrogen atoms. We also investigate the response of the CNT + GN rotor with higher values of q , namely $q = 5$ or 10.

Fig. 7(a) shows the final response of the rotor with respect to different values of q . It is evident that the CNT and GN in the rotor always have the same rotational speed. Those speeds increase continuously, i.e., without any jump, before 3000 ps. The reason is that the GN lacks sufficient curvature to wind onto the CNT or to unwind and leave the CNT when there are no more than 2 lines of C–H bonds. The fact that the potential of the rotor increases slightly (black and orange lines in Fig. 7(b)) indicates that the shape of the

GN changes slightly during rotation with the CNT.

When q is greater than 3, e.g., $q = 5$ or 10, the rotational speed of the rotor exhibits three jumps (Fig. 7(a)), and correspondingly, two traps appear in the history curves of the potential of the rotor. For the same reason, that is, winding of the GN into a CNS, the first jump occurs during [0, 42] ps when $q = 5$ or during [0, 30] ps when $q = 10$ (see Table 2). Also unwinding of the GN from CNS to nanoribbon causes the second jump during [778, 850] ps for $q = 5$ or during [885, 1000] ps for $q = 10$. To illustrate the mechanism for the third jump, in Fig. 7(b) we insert 5 snapshots of the configuration of the rotor (with CNT and GN). After 929 ps (the second jump), the potential of the rotor drops again. From the configuration of the rotor at 1498 ps, it is evident that the drop of potential is caused by new curling of the C–H area in the GN and even some portion of the GN being attracted to the CNT. With the acceleration of the rotor's rotation (or that of both CNT and GN), the tension within the GN nanoribbon increases. When the rotational frequency of the rotor reaches ~27 GHz, the curved part of the GN is stretched into a smooth nanoribbon again, and the potential jumps up. Later, the nanoribbon becomes flatter with the higher rotational speed of the rotor.

Comparing the durations from the second to the third jumps of potential of the GN with 5 and 10 lines of C–H bonds, we find that the second jump for $q = 5$ occurs earlier than that for $q = 10$. The reason is that the greater number of C–H bonds in the GN leads to a higher curvature of the GN and stronger interaction between GN and CNT (see Fig. 8(a) and (b)). Therefore, a higher rotational speed of the rotor is required for the second jump or for unwinding of the GN from CNS to nanoribbon. When the rotor is driven to rotate by the same stator, a longer acceleration time is necessary to reach the critical angular velocity. In contrast, the third jump for $q = 5$ occurs during [2125, 2200] ps, later than the third jump for $q = 10$ that occurs during [2065, 2150] ps (see Table 2). The reason is that the width of the unwound part of GN for $q = 5$ (Fig. 8(c)) is greater than that for $q = 10$ (Fig. 8(d)), indicating that the moment of inertia of the rotor for $q = 5$ is higher than that for $q = 10$. Therefore, a longer time is required for the rotor's rotational speed to approach its critical value when $q = 5$.

From the above, we conclude that the variation of the rotor's configuration is determined by q , that is, the number of lines of C–H bonds in the GN. If $q < 3$, the C–H bonds cannot produce enough curvature of the GN nanoribbon, so the nanoribbon cannot wind into a CNS. If q is 5 or more, the rotor may experience more than one jump in rotational frequency.

3.4. Effects of GN width on jumps in configuration of rotor

Intuitively, the GN width should influence the configuration variation of the "CNT + GN" rotor when the GN nanoribbon has more than 3 lines (parallel axis of inner tube) of C–H bonds near the contact side. The reason is that a longer nanoribbon can more easily produce a higher drop in potential of the rotor when the GN nanoribbon is winding into a CNS.

Fig. 9 demonstrates the rotational frequency and VPE of a rotor driven by the stators shown in Fig. 1. When the GN nanoribbon width is 5.8 nm, only two jumps of the dynamic response of the rotor occur. The first jump (down), occurring during [0, 23] ps, is caused by the winding of GN nanoribbon onto the CNT to reduce the potential energy of the rotor (top layer in Fig. 9(b)). The second jump, occurring during [615, 657] ps, is due to the unwinding of GN from the CNT. Later, the rotor rotates like a second hand on a clock. The result is very similar to that of the rotor with the GN width of 8.4 nm that has 3 lines of C–H bonds near the contact side (see Fig. 4). Hence the conclusion can be drawn that if we need the GN in a rotor to experience full expansion after unwinding (second jump),

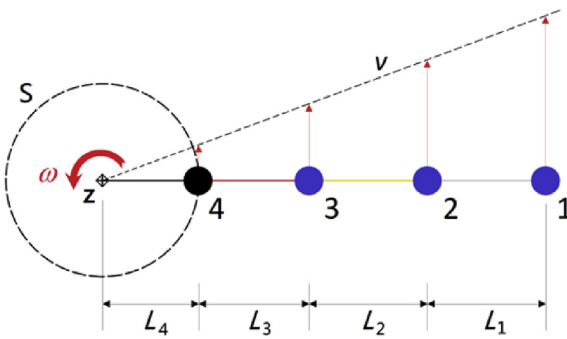


Fig. 6. Diagram of a multi-body rotational system. Ball No. 4 (black) rotates on the path "S" with the circle center of point "z", the rotational angular velocity is ω . Balls No. 1, 2, and 3 are connected one after another. The masses of the four balls are m_1 , m_2 , m_3 , and m_4 , respectively. The moment of inertia of the system is $I_z = \sum_{i=1}^4 m_i (\sum_{j=i}^4 L_j)^2$ and the stretching force between two neighboring balls, e.g., i and $(i+1)$, can be calculated by $F_{i(i+1)} = (\sum_{j=1}^i m_j) L_j \omega^2 + F_{(i-1)i}$, ($i = 1, 2, \dots$). (A colour version of this figure can be viewed online.)

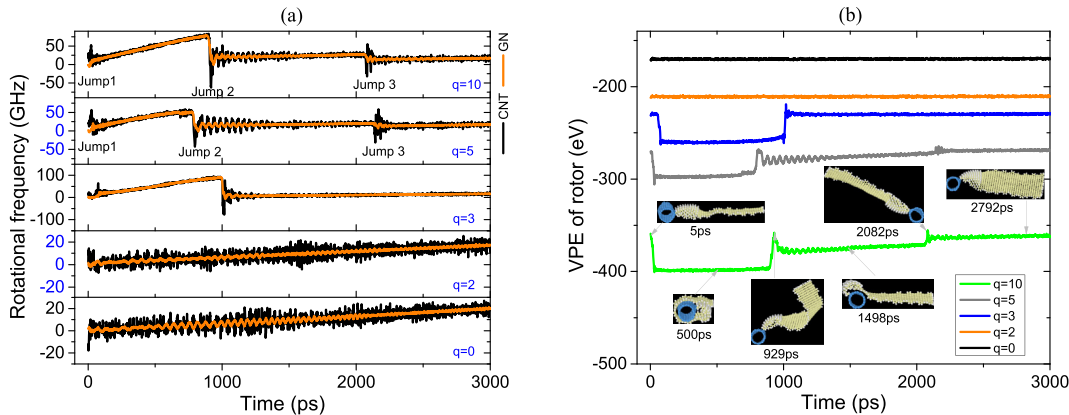


Fig. 7. Dynamic response of the “CNT + GN” rotor driven by 4-IRD-atom stators. The GN width is 8.4 nm and the GN has 5 schemes of C–H bond layout. (a) Histories of rotational frequency of CNT (black line) and GN (orange line); (b) histories of potential energy for the system with the same reference value of −21,000 eV (black line: $q = 0$; orange line: $q = 10$; blue line: $q = 3$; grey line: $q = 5$; yellow line: $q = 10$). (A colour version of this figure can be viewed online.)

Table 2

Dynamic response of GN for the three configuration jumps (in Fig. 7) of the rotor with respect to $q = 5$ and 10.

$q = 5$				$q = 10$		
	Jump 1	Jump 2	Jump 3	Jump 1	Jump 2	Jump 3(MovieM3)
Duration (ps)	[0, 42]	[778, 850]	[2125, 2200]	[0, 30]	[885, 1000]	[2065, 2150]
Rotat. Freq. (GHz)	from 0 to 10	from 50 to 15	from 20 to 13	from 0 to 10	from 77 to 20	from 27 to 12
VPE (eV)	-26	+17	+2	-40	+19	+8

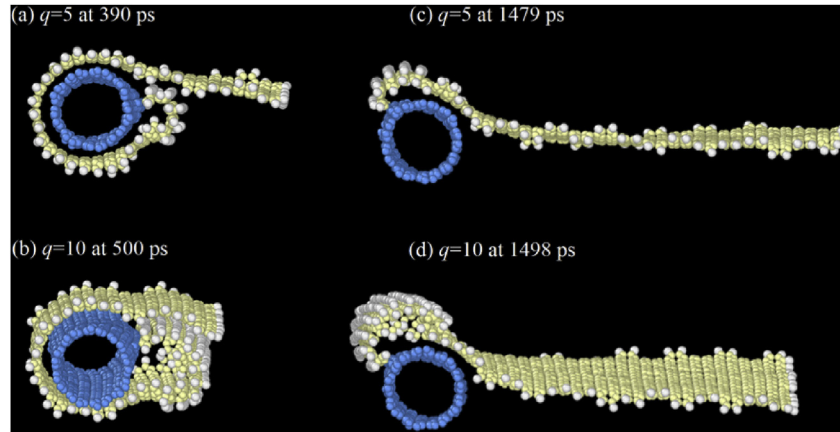


Fig. 8. Four configurations of the rotor before the second and third jumps. (a) at 390 ps, i.e., before unwinding of the GN with 5 lines (parallel axis of inner tube) of C–H bonds ($q = 5$); (b) at 500 ps, i.e., before unwinding of the GN with 10 lines of C–H bonds; (c) at 1479 ps, i.e., before full expansion of the GN with $q = 5$; (d) at 1498 ps, i.e., before full expansion of the GN with $q = 10$. (A colour version of this figure can be viewed online.)

we can choose between either a shorter GN with more C–H bond lines or a longer GN nanoribbon with fewer lines of C–H bonds.

Comparing the three histories of the rotational frequency of the rotor in Fig. 9, we find that 2, 3, and 4 jumps occur in the rotors, corresponding to GN nanoribbon widths of 5.8 nm, 8.4 nm, and 14.8 nm, respectively, if the GNs have the same C–H bond layout scheme. In particular, the VPE of the rotor with the GN width of 14.8 nm approaches zero after the fourth jump in configuration during [6400, 6544] ps (Fig. 9(b)). This result also implies that the GN is almost fully flattened after the last jump. We also find that the rotational frequency of the rotor with the GN width of 14.8 nm is the lowest among the three models. This is because that GN has the highest moment of inertia.

If we set $q = 3$, that is, there are 3 lines (parallel axis of inner

tube) of C–H bonds in the GN near the contact side, the dynamic response of the rotor is different from that of the rotor with 5 lines (parallel axis of inner tube) of C–H bonds (shown in Fig. 9). We select five models of the rotor with different GN nanoribbon widths of 4.5, 5.4, 5.8, 8.4, and 14.8 nm. The dynamic responses of the rotors are shown in Fig. 10. As there are only 3 lines of C–H bonds in the GN, the number of jumps for the configurations of the rotors with GN nanoribbon widths of 8.4 and 14.8 nm is one less than that of the GN with 5 lines of C–H bonds. When the width of GN nanoribbon is either 5.4 or 5.8 nm, there is no jump, as evident in the VPE history curves of the rotors shown in Fig. 10(b).

If we reduce the GN width further, e.g., to 4.5 nm, there are three jumps. The first jump is due to the winding of the GN on the CNT (Movie M4). The second jump occurs because of the unwinding of

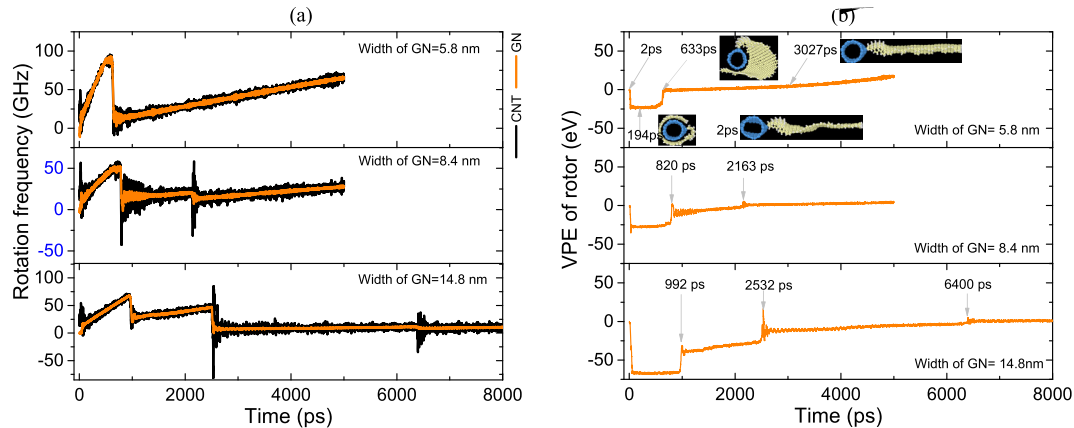


Fig. 9. Dynamic responses of the CNT and GN in system driven by stators shown in Fig. 1. There are 5 lines of C–H bonds in GN of different widths. (a) Histories of rotational frequency of CNT + GN with width of 5.8 or 8.4 or 14.8 nm; (b) histories of VPE of the rotor; the reference values are $-18,109.1$, $-21,270.1$, and $-29,170.7$ eV for the rotors with GN widths of 5.8, 8.4, and 14.8 nm, respectively. (A colour version of this figure can be viewed online.)

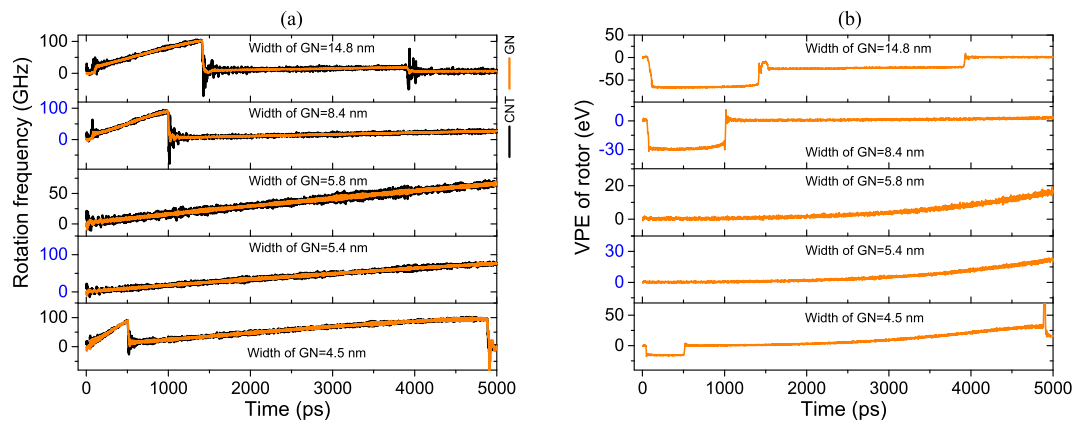


Fig. 10. Dynamic responses of the CNT and GN in system driven by stators shown in Fig. 1. There are 3 lines of C–H bonds in the GN with different widths. (a) Histories of rotational frequency of CNT and GN; (b) histories of VPE of the rotor; the reference values are $-16,489.4$, $-17,543.1$, $-18,069.9$, $-21,230.8$, and $-29,132.3$ eV for the rotors with GN widths of 4.5, 5.4, 5.8, 8.4, and 14.8 nm, respectively. (A colour version of this figure can be viewed online.)

the GN into a nanoribbon, and the third jump is actually caused by breakage of the CNT (Movie M5). The major reason for the first jump in configuration is that the axial free side of the GN is closer to the CNT in comparison with the other models and is drawn tightly onto the CNT. Hence, the winding of GN onto the CNT is sensitive to the width of the GN nanoribbon and the number of lines of C–H bonds in the GN.

3.5. Effects of stator on configuration jumps of rotor

From Fig. 3, we know that the rotor's acceleration increases when the rotor is driven by a stator with more atoms with IRD. To demonstrate the effects of the stator on variation of the rotor configuration, we choose two types of stator to drive the rotation of the 14.8 nm width GN nanoribbon with the same C–H bonds layout scheme, with $q = 5$ in the present simulation.

From Fig. 11, we find that the two rotors have the same number of jumps in configuration. However, except for the first jump, the jumps of the rotor driven by 2-IRD-atom stators occur correspondingly later than those of the rotor driven by 4-IRD-atom stators. The time and the values of rotational frequency and VPE of the rotor for the jumps are listed in Table 3. We find that the differences at each jump are very small between the rotational frequencies and the VPEs of the rotors driven by the two types of

stator. The rotational frequency of the GN after the last jump is ~ 8.5 GHz driven by the 2-IRD-atom stator or ~ 8.7 GHz by the 4-IRD-atom stator. Comparison of the inserted snapshots for the configurations of the rotors in Fig. 11(b) shows that the configuration variations of the rotors are similar when they are driven to rotate by different stators. We can therefore draw the conclusion that the number of atoms with IRD on the stator only affects the time at which the jump occurs.

4. Conclusions

To find a feasible method for measuring the rotation of the rotor in a DWCNT-based nanomotor driven by a uniform temperature field, we suggest a complex rotor made from a SWCNT bonded with a rectangular GN nanoribbon. From simulation results, some remarkable conclusions are drawn:

- (1) To build a variable configuration of the “CNT + GN” motor, the GN nanoribbon should first be wound on the CNT. Hence, at least 3 lines of C–H bonds should be arranged on the GN near the side adjacent to the tube;
- (2) Configuration jumps (corresponding to unwinding of the GN) of the “CNT + GN” rotor can occur when the rotor's rotational speed reaches critical values. After a configuration

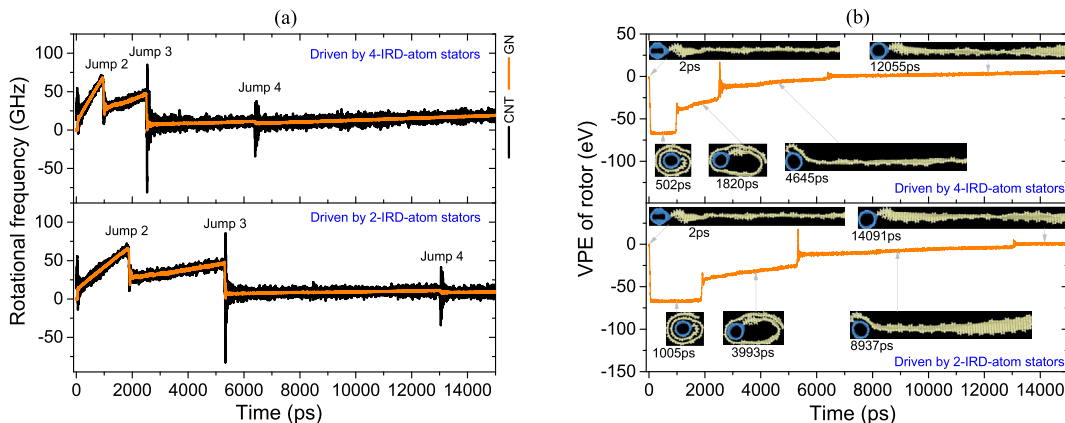


Fig. 11. Dynamic response of the CNT and GN in system driven by either 2- or 4-IRD-atom stators. The GN nanoribbon width is 14.8 nm and there are 5 lines of C–H bonds. (a) Histories of rotational frequency of CNT and GN; (b) histories of VPE of rotor driven by two types of stator, with reference values of −29170.7 eV for the 4-IRD-atom stators and −29,171 eV for the 2-IRD-atom stators. Typical snapshots of the rotor are inserted. (A colour version of this figure can be viewed online.)

Table 3

Dynamic response of GN for the three configuration jumps (in Fig. 11) of the rotors driven by 2- or 4-IRD-atom stators.

	2-IRD-atom			4-IRD-atom		
	Jump 2	Jump 3	Jump 4	Jump 2	Jump 3	Jump 4
Duration (ps)	[1870, 1990]	[5289, 5400]	[13,025, 13,100]	[960, 1080]	[2480, 2680]	[6400, 6544]
Rotat. Freq. (GHz)	from 65 to 28	from 47.5 to 7	from 11 to 8.5	from 67 to 28	from 47 to 7	from 11.2 to 8.7
VPE (eV)	+18	+13	+3	+23	+13	+2

jump, the rotor's rotational speed drops to a few GHz, facilitating measurement of the rotation;

- (3) Due to the high local curvature of GN, more configuration jumps of the rotor can occur when more C–H bonds are arranged on a GN nanoribbon with higher width. After full expansion of the GN nanoribbon, the variation of the system's potential energy reaches zero, a feature that also provides a clue for finding configuration jumps;
- (4) On the stator, more atoms with the same IRD will reduce the duration between two adjacent configuration jumps of the same rotor. But the number of atoms with the same IRD has no influence on either the number of jumps or the variation of the rotor's rotational frequency.

To measure the rotation of the rotor, we can adjust such factors as the number of IRD atoms, the width of the GN nanoribbon, and the C–H bonding scheme.

Acknowledgments

The authors are grateful for the financial support from the National Natural Science Foundation of China (Grant No. 11372100).

References

- [1] H.W. Kroto, J.R. Heath, S.C. O'Brien, R.F. Curl, R.E. Smalley, C60: buckminsterfullerene, *Nature* 318 (6042) (1985) 162–163.
- [2] S. Iijima, Helical microtubules of graphitic carbon, *Nature* 354 (1991) 56–58.
- [3] H. Shioyama, T. Akita, A new route to carbon nanotubes, *Carbon* 41 (1) (2003) 179–181.
- [4] E. Perim, R. Paupitz, D.S. Galvao, Controlled route to the fabrication of carbon and boron nitride nanoscrolls: A molecular dynamics investigation, *J. Appl. Phys.* 113 (5) (2013) 054306.
- [5] K.S. Novoselov, A.K. Geim, S.V. Morozov, D. Jiang, Y. Zhang, S.V. Dubonos, et al., Electric field effect in atomically thin carbon films, *Science* 306 (2004) 666–669.
- [6] Y. Zhu, S. Murali, W.W. Cai, X.S. Li, J.W. Suk, J.R. Potts, R.S. Ruoff, Graphene and graphene oxide: synthesis, properties, and applications, *Adv. Mater.* 22 (35) (2010) 3906–3924.
- [7] C.D. Reddy, Y.W. Zhang, V.B. Shenoy, Patterned graphene—a novel template for molecular packing, *Nanotechnology* 23 (16) (2012) 165303.
- [8] S. Zhu, T. Li, Hydrogenation-assisted graphene origami and its application in programmable molecular mass uptake, storage, and release, *ACS nano* 8 (3) (2014) 2864–2872.
- [9] Z. Qin, Q.H. Qin, X.Q. Feng, Mechanical property of carbon nanotubes with intramolecular junctions: molecular dynamics simulations, *Phys. Lett. A* 372 (44) (2008) 6661–6666.
- [10] J. Cumings, A. Zettl, Low-friction nanoscale linear bearing realized from multiwall carbon nanotubes, *Science* 289 (5479) (2000) 602–604.
- [11] R.F. Zhang, Z.Y. Ning, Y.Y. Zhang, Q.S. Zheng, Q. Chen, H.H. Xie, Q. Zhang, W.Z. Qian, F. Wei, Superlubricity in centimetres-long double-walled carbon nanotubes under ambient conditions, *Nat. Nanotechnol.* 8 (12) (2013) 912–916.
- [12] K. Kim, X. Xu, J.H. Guo, D.L. Fan, Ultrahigh-speed rotating nanoelectromechanical system devices assembled from nanoscale building blocks, *Nat. Commun.* 5 (2014) 3632.
- [13] J. Pekarek, R. Vrba, J. Prasek, O. Jasek, P. Majzlikova, J. Pekarkova, L. Zajickova, MEMS carbon nanotubes field emission pressure sensor with simplified design: performance and field emission properties study, *IEEE Sensors J.* 15 (3) (2015) 1430–1436.
- [14] A. Barreiro, R. Rurali, E.R. Hernández, J. Moser, T. Pichler, L. Forró, A. Bachtold, Subnanometer motion of cargoes driven by thermal gradients along carbon nanotubes, *Science* 320 (5877) (2008) 775–778.
- [15] H.A. Zambrano, J.H. Walther, R.L. Jaffe, Thermally driven molecular linear motors: a molecular dynamics study, *J. Chem. Phys.* 131 (24) (2009) 241104.
- [16] I. Santamaría-Holek, D. Reguera, J.M. Rubí, Carbon-nanotube-based motor driven by a thermal gradient, *J. Phys. Chem. C* 117 (6) (2013) 3109–3113.
- [17] S. Zhang, W.K. Liu, R.S. Ruoff, Atomistic simulations of double-walled carbon nanotubes (DWNTs) as rotational bearings, *Nano Lett.* 4 (2) (2004) 293–297.
- [18] W. Qiu, Y.L. Kang, Z.K. Lei, Q.H. Qin, Q. Li, A new theoretical model of a carbon nanotube strain sensor, *Chin. Phys. Lett.* 26 (8) (2009) 080701.
- [19] W. Qiu, Y.L. Kang, Z.K. Lei, Q.H. Qin, Q. Li, Q. Wang, Experimental study of the Raman strain rosette based on the carbon nanotube strain sensor, *J. Raman Spectrosc.* 41 (10) (2010) 1216–1220.
- [20] J. Feng, W. Li, X.F. Qian, J.S. Qi, L. Qi, J. Li, Patterning of graphene, *Nanoscale* 4 (16) (2012) 4883–4899.
- [21] Z.C. Tu, X. Hu, Molecular motor constructed from a double-walled carbon nanotube driven by axially varying voltage, *Phys. Rev. B* 72 (3) (2005) 033404.
- [22] B. Wang, L. Vuković, P. Král, Nanoscale rotary motors driven by electron tunneling, *Phys. Rev. Lett.* 101 (18) (2008) 186808.
- [23] M. Hamdi, A. Subramanian, L.X. Dong, A. Ferreira, B.J. Nelson, Simulation of rotary motion generated by head-to-head carbon nanotube shuttles, *Mechatronics*, *IEEE/ASME Trans.* 18 (1) (2013) 130–137.
- [24] J.W. Kang, H.J. Hwang, Nanoscale carbon nanotube motor schematics and

- simulations for micro-electro-mechanical machines, *Nanotechnology* 15 (11) (2004) 1633.
- [25] A. Prokop, J. Vacek, J. Michl, Friction in carborane-based molecular rotors driven by gas flow or electric field: Classical molecular dynamics, *ACS nano* 6 (3) (2012) 1901–1914.
- [26] Z. Xu, Q.S. Zheng, G. Chen, Thermally driven large-amplitude fluctuations in carbon-nanotube-based devices: molecular dynamics simulations, *Phys. Rev. B* 75 (19) (2007) 195445.
- [27] K. Cai, Y. Li, H. Yin, Q.H. Qin, Gradientless temperature-driven rotating motor from a double-walled carbon nanotube, *Nanotechnology* 25 (50) (2014) 505701.
- [28] H. Yin, K. Cai, Unwinding of a carbon nanoscroll due to high speed rotation, *AIP Adv.* 5 (10) (2015) 107202.
- [29] LAMMPS, Molecular Dynamics Simulator, 2015. <http://lammps.sandia.gov/>.
- [30] S. Plimpton, Fast parallel algorithms for short-range molecular dynamics, *J. Comp. Phys.* 117 (1995) 1–19.
- [31] S.J. Stuart, A.B. Tutein, J.A. Harrison, A reactive potential for hydrocarbons with intermolecular interactions, *J. Chem. Phys.* 112 (14) (2000) 6472–6486.
- [32] Y.F. Guo, W.L. Guo, Soliton-like thermophoresis of graphene wrinkles, *Nano-scale* 5 (1) (2013) 318–323.
- [33] J.G. Chen, Y. Gao, C.L. Wang, R.L. Zhang, H. Zhao, H.P. Fang, Impeded mass transportation due to defects in thermally driven nanotube nanomotor, *J. Phys. Chem. C* 119 (30) (2015) 17362–17368.
- [34] Q.X. Pei, Y.W. Zhang, V.B. Shenoy, A molecular dynamics study of the mechanical properties of hydrogen functionalized graphene, *Carbon* 48 (3) (2010) 898–904.
- [35] C. Reddy, Y.W. Zhang, Structure manipulation of graphene by hydrogenation, *Carbon* 69 (2014) 86–91.
- [36] P.A.S. Autreto, J.M. de Sousa, D.S. Galvao, Site-dependent hydrogenation on graphdiyne, *Carbon* 77 (2014) 829–834.
- [37] Z. Guo, T. Chang, X. Guo, H. Gao, Thermal-induced edge barriers and forces in interlayer interaction of concentric carbon nanotubes, *Phys. Rev. Lett.* 107 (2011) 105502.
- [38] K. Cai, J. Yu, H. Yin, Q.H. Qin, Sudden stoppage of rotor in a thermally driven rotary motor made from double-walled carbon nanotubes, *Nanotechnology* 26 (9) (2015) 095702.
- [39] C. Zhu, W.L. Guo, T.X. Yu, Energy dissipation of high-speed nanobearings from double-walled carbon nanotubes, *Nanotechnology* 19 (46) (2008) 465703.
- [40] A.A. Dzhurakhalov, F.M. Peeters, Structure and energetics of hydrogen chemisorbed on a single graphene layer to produce graphane, *Carbon* 49 (10) (2011) 3258–3266.